

IMAGING OF CO AND CO₂ USING INFRARED PLANAR LASER-INDUCED FLUORESCENCE

BRIAN J. KIRBY AND RONALD K. HANSON

*Mechanical Engineering Department
Stanford University
Stanford, CA 94305-3032, USA*

Infrared (IR) planar laser-induced fluorescence (PLIF) techniques for imaging of carbon monoxide and carbon dioxide are reported. These diagnostics employ a tunable IR source to excite overtone and combination band transitions of CO and CO₂, respectively, and one or two InSb focal plane arrays to collect fluorescence emitted via fundamental transitions from excited vibrational states. A brief outline of the theoretical framework for absorption and fluorescence modeling is presented, with most attention paid to the distinct characteristics stemming from the use of vibrational (IR) transitions as compared to more traditional electronic (UV) transitions. Of note are the conclusions that (1) acceptable fluorescence quantum yield (and therefore signal level) can be achieved despite relatively small Einstein *A* coefficients, as the quenching processes following IR excitation are often slow; and (2) vibration-to-vibration transfer to other IR-active species can enable imaging of more than one species with a single excitation wavelength. Experimentally, the large dynamic range afforded by the IR cameras (14 bit) allows for effective imaging despite the presence of background luminosity, while the use of two cameras enables imaging of multiple species simultaneously and/or common-mode rejection of luminous background in unsteady flows. PLIF imaging of CO and CO₂ is demonstrated for room-temperature mixing processes with signal-to-noise ratio = 1 detection limits near 1000 ppm. Imaging of both CO and CO₂ in a steady laminar coflowing CO/Ar/H₂ flame is also presented using laser excitation of CO only.

Introduction

Infrared imaging diagnostics have undergone rapid expansion in recent years, due primarily to improved performance of IR focal plane arrays (FPAs). Improved FPAs, combined with more powerful and more robust tunable IR laser sources, have made it possible to demonstrate planar laser-induced fluorescence (PLIF) imaging diagnostics in the IR [1]. While PLIF imaging is well established as a diagnostic technique using UV or visible photons to excite electronic transitions [2,3], many key species exist that are undetectable by traditional PLIF diagnostics because their electronic transitions lie in the vacuum UV and, therefore, cannot be used for single-photon PLIF techniques. These species include but are not limited to important combustion species such as CO, CO₂, CH₄, and H₂O, each of which has a strong IR spectral signature.

Competing diagnostics for imaging of species that lack convenient UV transitions include spontaneous Raman scattering [4,5] and multiphoton (nonlinear) PLIF techniques. Raman is linear and easily modeled but generates weak signals and can be limited in implementation by a variety of spectral interferences; multiphoton LIF, despite its usefulness for point measurements [5] and imaging [6] of CO in

flames, suffers (for most species, such as H₂O [7]) from strong nonlinearity and low signal due to the predissociative nature of the excited state. In contrast to Raman and multiphoton techniques, IR PLIF is a *linear* technique that offers higher signal levels than Raman (several orders more signal photons) and is applicable to all IR-active species including CH₄, CO₂, and H₂O. High signal levels imply high SNR and dynamic range while linearity permits easy interpretation of data and increased quantitative accuracy. Fig. 1 shows two sample experimental realizations (discussed in detail later in the paper) of single-shot IR PLIF imaging of CO and CO₂ in flame and room temperature conditions, respectively. The quality of these images serves to indicate the potential for IR PLIF to provide spatially and temporally resolved imaging of CO and CO₂ in flows pertinent to combustion. Previous work has reported initial imaging efforts for CO [1]; the present study continues and builds upon those efforts, presenting new results with both single- and dual-camera techniques for imaging of CO and CO₂ in steady and unsteady flows of interest to the combustion community. The following sections will present theory, experimental techniques, and demonstration experiments for infrared PLIF imaging of CO and CO₂.

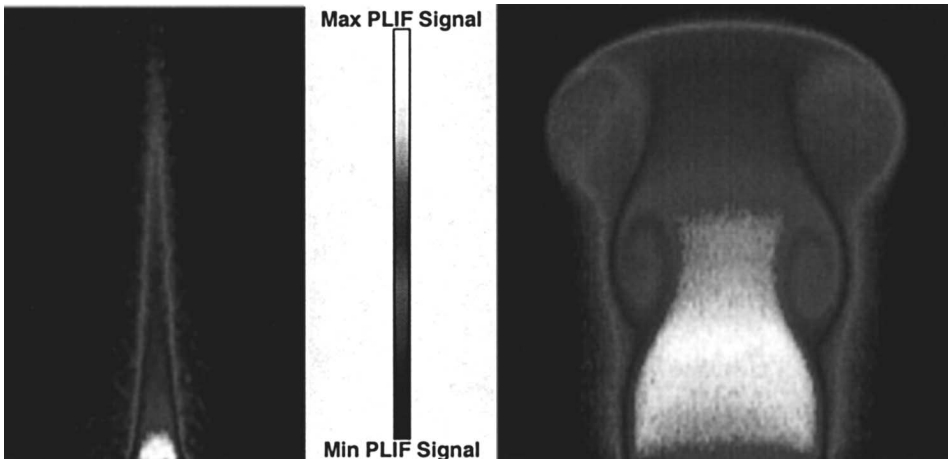


FIG. 1. Single-shot CO and CO₂ IR PLIF images. CO at left indicates the fuel region of a steady laminar coflowing CO/H₂-air flame. CO₂ at right is a forced room-temperature jet issuing into air.

Theory

PLIF Equation

The fluorescence equation for PLIF imaging with weak excitation can be written as

$$S_f = \frac{E}{h\nu} gSl \frac{P\chi_{\text{abs}}}{kT} \phi\eta_c \quad (1)$$

where S_f (photons per camera pixel) is the fluorescence signal; E (J) is the laser pulse energy incident on the imaged pixel volume; $h\nu$ (J) is the energy per photon; g (cm) is the convolution of the laser and absorption lineshapes; S (cm) is the line strength per number density, which takes into account the Boltzmann fraction of the absorbing species in the lower state of the laser transition; l (cm) is the length of the area imaged onto the pixel; $P\chi_{\text{abs}}/kT$ (cm⁻³) is the number density of the species; ϕ is the fluorescence quantum yield; and η_c is the collection efficiency of the optics and camera. The fluorescence signal for isobaric flows is a function of imaged species mole fraction, bath gases (through energy transfer rates and their effect on fluorescence yield), and temperature (through energy transfer rates, number density, and state distributions). For species imaging, short exposure times can be used to minimize sensitivity to collisional environment, while judicious choice of excitation line can be used to control temperature dependence.

The strengths of vibrational molecular transitions (which determine the line strength S and are a component of the fluorescence yield ϕ) are weak as compared to electronic transitions; however, this weakness is offset in certain situations by the large mole fractions present for the species of interest (e.g., CO, CO₂) in typical flows as well as the slow nature of

typical de-excitation processes which limit the fluorescence yield ϕ .

Fluorescence Quantum Yield

The parameters in equation 1 are easily quantified, with the possible exception of the fluorescence yield ϕ , which may be written as an integration of the relevant excited state populations and spontaneous emission coefficients over the camera integration time:

$$\phi = \sum_j \int_0^\tau A_j \frac{n_j(t)}{N} dt \quad (2)$$

Here, fluorescence is summed over j excited states. A_j is the summed Einstein A coefficient for all emitting transitions from the state j consistent with the spectral collection bandwidth, n_j/N is the instantaneous population in the excited state normalized by the total number of absorbed laser photons, and τ is the camera integration time.

Differences in scale between the camera integration time and the emissive state radiative and collisional lifetimes lead to simpler expressions that describe the limiting behavior of equation 2. For traditional PLIF techniques, which employ electronic transitions, the excited state population undergoes simple exponential decay dictated by the collisional quench rate Q , since the collisional quenching is typically fast (~ 1 ns) when compared to either the radiative lifetime (~ 1 μ s) or the camera gate time (~ 20 – 300 ns). In this case, we recover the familiar equation for fluorescence yield:

$$\phi = A/Q \quad (3)$$

Equation 3, though, typically does *not* properly describe the fluorescence yield for IR PLIF techniques, because the vibration-to-translation (V-T)

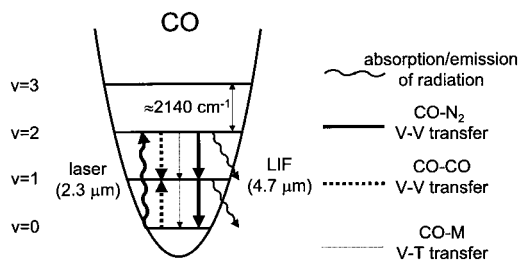


FIG. 2. Energy transfer diagram for CO molecules during CO LIF.

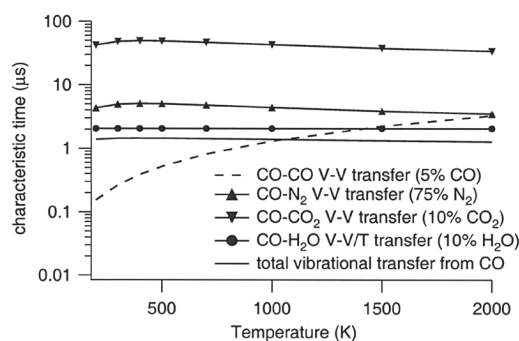


FIG. 3. Calculated characteristic times ($1/\text{transfer rate}$) of VET from CO to common species as a function of temperature at 1 atm. Components which remove energy from CO are shown with symbols, and the total transfer is summed as the solid line. The dashed line indicates CO-CO V-V transfer which tends to equilibrate the CO vibrational mode but does not serve as a quenching mechanism.

energy transfer which serves to remove vibrational energy from the system is often slow ($\sim 1\text{--}100\ \mu\text{s}$) as compared to the camera integration time ($\sim 0.1\text{--}10\ \mu\text{s}$). Vibration-to-vibration (V-V) energy transfer is often fast but serves only to rearrange the vibrational energy and does not provide strong coupling to the translational and rotational modes. Thus, as the camera integration time is shortened below the V-T decay time, the limit is approached in which the excited state population stays constant during the camera integration time. In this case, equation 2 approaches

$$\phi = A\tau \quad (4)$$

This limit is advantageous because fluorescence quantum yield becomes independent of excited state de-excitation rates and is therefore independent of both bath gas and temperature.

We turn now to a more detailed examination of the general energy transfer processes described above. Following laser excitation, typically the pumped vibrational mode equilibrates itself first, followed by intermolecular V-V equilibration with near-resonant modes of similar energy (e.g., CO, N₂, v₃

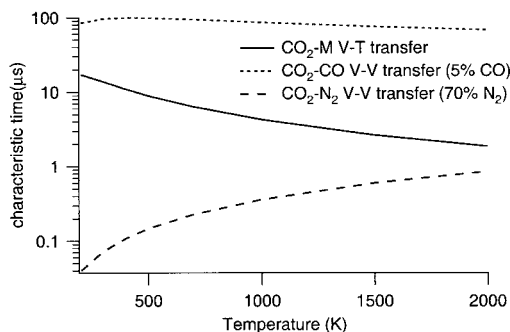


FIG. 4. Calculated characteristic times ($1/\text{transfer rate}$) of VET from CO₂ to common species as a function of temperature at 1 atm.

of CO₂), followed by relatively slower V-V/T equilibration with nonresonant vibrational modes and the translational/rotational modes. Collisional depletion of the pumped mode (and coupled modes emitting within the collection bandwidth) competes with spontaneous emission to determine the fluorescence quantum yield. A schematic diagram of these energy transfer processes is shown in Fig. 2.

Characteristic times for vibrational energy transfer (VET) from CO to common species for 1 atm and typical concentrations are shown in Fig. 3. Since CO has only one vibrational frequency and rather large energy spacing, species without near-resonant modes (e.g., inert gases, O₂) play little role in extracting energy from CO at these temperatures and are therefore not shown. Temperature dependences are minor, as expected, due to the dominance of near-resonant V-V transfer mechanisms which stem in large part from long-range interactions rather than energetic collisions.

For CO₂, which has three vibrational frequencies and smaller vibrational spacing, energy transfer occurs both via near-resonant transfer (upon collisions with CO and N₂) and via non-resonant intermodal V-V transfer (upon collisions with any molecule M), both of which serve to deplete states with asymmetric stretch (v₃). Because of the efficiency of intermodal V-V transfer (defined here as transfer of energy between modes, e.g., the transfer caused by a collisional CO₂(00⁰1) → CO₂(11¹0)_I transition), the energy gaps associated with the vibrational transfer mechanisms are smaller, and energy resonance plays a less important role in dictating the relative speed of different VET mechanisms. Because energy resonances are less important, rates of energy transfer are less dependent on the species makeup of the bath gas.

Characteristic times for VET from CO₂ to common species at typical concentrations are shown in Fig. 4. The primary energy transfer processes are resonant transfer with N₂ and collisional intermodal V-V transfer. Temperature dependences are stronger

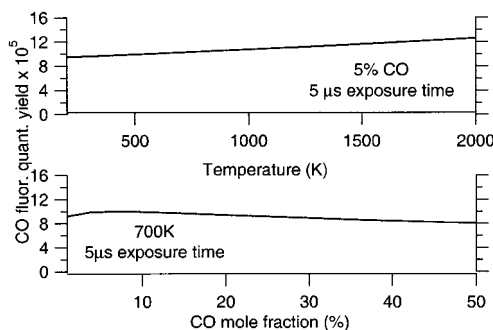


FIG. 5. CO fluorescence quantum yield as a function of temperature and composition for the simplified case of CO in N_2 .

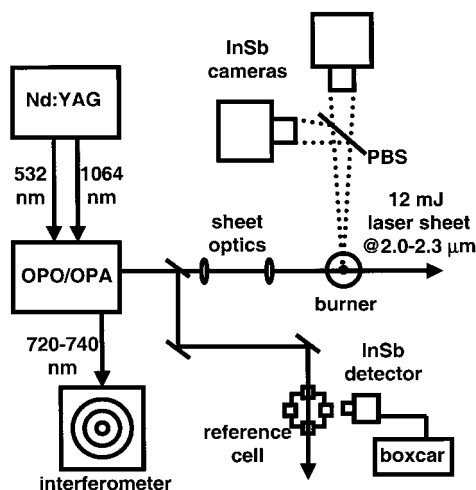


FIG. 6. Experimental setup for imaging experiments. PBS, pellicle beamsplitter. InSb cameras (Santa Barbara Focalplane SBF134) have the following characteristics: 0.7–5.3 μm sensitivity range; 30 μm pixels; 85% quantum efficiency; 130 ns minimum integration time setting; 300 Hz maximum frame rate.

for CO_2 due to the nonresonant nature of the intermodal V-V transfer, which is therefore more dependent on collision energy.

A model of the vibrational energy transfer has been developed so as to quantify ϕ as a function of bath gas, temperature, pressure, and camera integration time. This model uses a rate equation formulation (CHEMKIN) to solve for the vibrational-state-specific populations as a function of time, including effects of both V-V and V-T processes. For simplicity, the model assumes translational and rotational equilibrium.

To enable implementation using the CHEMKIN interface and solver, functions are fit to experimental or computational reaction rate data from a variety of

references: for CO + M V-T transfer, Refs. [8–12]; for CO–CO V-V transfer, Refs. [12,13]; for CO– N_2 V-V transfer, Refs. [9,14,15]; for CO– CO_2 V-V transfer, Refs. [16–20]; for CO– O_2 V-V transfer, Ref. [10]; for CO_2 –M V-T (and collisional intermodal V-V) transfer, Refs. [18,20–26]; for CO_2 – CO_2 V-V transfer, Ref. [22]; for CO_2 – N_2 V-V transfer, Refs. [18,19]; for N_2 – N_2 V-V transfer, Ref. [27]; and for O_2 – O_2 V-V transfer, Ref. [28]. When necessary (rarely), literature results are extrapolated using Schwartz-Slawsky-Herzfeld theory. The thermodynamic database input to CHEMKIN is modified slightly to treat the molecules on a vibrational-state-specific basis.

A simple example of fluorescence quantum yield calculations is shown in Fig. 5 for CO using a 5 μs exposure time. This example highlights the advantages of using exposure times that are shorter than excited state lifetime. In addition to being desirable for time resolution and reduction of background luminosity, short exposures cause ϕ to approach the limit of equation 4 and thus lead to a fluorescence quantum yield that is only a weak function of composition and temperature (in contrast, if the exposure time is long, ϕ for pure CO is several orders of magnitude higher than 50% CO in N_2). For this exposure time, variations in fluorescence quantum yield are minor ($\pm 10\%$) over the rather wide ranges presented and are similarly minor for the experimental conditions considered in this paper. With an exposure time of 1 μs and the same conditions, these variations can be kept below $\pm 3\%$. In complicated flowfields where detailed calculations of fluorescence yield are difficult or impossible, quantitative *a priori* calculations of ϕ may be made feasible through use of short exposure times.

Imaging Setup and Techniques

The experimental setup used for imaging is shown in Fig. 6 and described in more detail in Ref. [1]. The tunable IR source (for convenience we refer to this system interchangeably as laser or optical parametric oscillator) is a 10 Hz, nanosecond-pulse system whose wavelength is controlled by a 532 nm pumped, grating-tuned optical parametric oscillator (Continuum Mirage 3000) and whose power is generated and amplified by four 1064 nm pumped optical parametric amplifier stages. Slight misalignment is used (in conjunction with the naturally occurring walkoff) to ensure that the mid-IR beam is divergent (large M^2 value) and thus focuses loosely and exhibits a large effective Rayleigh range. This misalignment induces minimal energy loss in the idler beams since precisely collinear alignment (with the pump powers and crystal lengths used in this work) leads to localized pump reconversion in the last crystal stage.

The oscillator signal beam (720–740 nm) from the laser is monitored using a commercial interferometer (Burleigh WA-4500) to ensure single-longitudinal-mode operation (400 MHz linewidth) and to

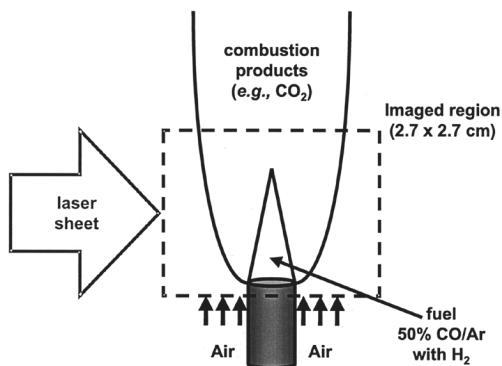


FIG. 7. CO/Ar/H₂ flame and imaged region.

determine the wavelength of the mid-IR beam. The laser is grating-tuned to absorption lines of overtone or combination bands of CO or CO₂ in the 2.0–2.4 μm region and centered on a specific line by maximizing LIF from a reference cell. The mid-IR beam is then expanded vertically and focused horizontally using calcium fluoride cylindrical lenses to generate a 4 cm high laser sheet with a 450 μm (full width at half maximum) waist, 50 mm Rayleigh range, and nominal pulse energy of 12 mJ. PLIF signal is collected through bandpass filters and $f/2.5$ singlet CaF₂ lenses onto one or two 256 \times 256 InSb cameras with submicrosecond gating capabilities (Santa Barbara Focalplane SBF 134). Typical imaged region sizes are roughly 2.5 \times 2.5 cm, and typical integration times range from 1 to 20 μs . The InSb cameras have been designed to provide short exposure times and are therefore capable of submicrosecond exposures without bias changes or other nonlinear effects common to many IR cameras.

Standard techniques as described in many other sources (Refs. [1,2,29]) are used to correct each image individually for laser attenuation, laser sheet inhomogeneity, and background signals of both optical and electrical nature. A strictly linear analysis is used (equation 1) which assumes negligible perturbation of the molecular state distribution. The validity of this approximation was verified by (1) detailed rate equation analysis using rotational energy transfer rates inferred from pressure-broadened linewidths and line mixing and (2) measurements of LIF linearity.

For each camera and filtering scheme, pixel-by-pixel responsivity and gain are calibrated by taking images of uniform temperature solid (Lambertian) graybody emitters. Errors caused by approximating these as isotropic sources were negligible for the collection optics used in this work but could be important if extremely fast optics are used.

For the results in this paper which involve two-camera imaging, care is taken to ensure that the two

images can be correctly matched to each other spatially. Here, techniques analogous to those in previous multicamera PLIF studies (e.g., Ref. [29] and references therein) are employed. Both cameras collect fluorescence from the same side of the image plane, and the fluorescence is split between the two cameras with a beamsplitter. A 2 μm pellicle is employed for this purpose so that the spatial separation of the two surface reflections at the focal plane ($<4 \mu\text{m}$) is much less than a pixel width (30 μm). Identical collection optics are employed at equal magnification, and the position of the two image planes are aligned to within approximately 1 pixel of each other. Test images of a heated wire mesh are taken with both cameras, and a spatial correlation between test images is used to transform one image onto another, correcting for any warping of the image plane caused by imperfections in the alignment, lenses, beamsplitters, and focal planes. Tests on this algorithm indicate that the images can be correlated to each other to within approximately 1/3 pixel; thus, the spatial dynamic range of multiple-camera images is only very slightly degraded by the use of the multicamera technique and the attendant transformations. Since our PLIF images are primarily read-noise limited, signal-to-noise ratio (SNR) losses associated with dual-image techniques are modest.

Imaging Experiments

Flow Test Cases

Two flow conditions are used in this work: (1) a 6 mm diameter, room-temperature, forced jet, in which a valve is quickly opened and closed, superimposing an impulse onto a laminar jet flow, thus forming one or more vortex rings; and (2) a laminar flame with 50% CO/50% Ar as fuel (trace H₂ added) with an air co-flow. This flame (Fig. 7) could be perturbed to explore unsteady effects as desired, although only steady results are presented here.

Excitation/Collection Schemes

Three excitation/collection schemes are employed: (1) excitation of CO via the ground state 2ν band near 4300 cm^{-1} (2.35 μm) and collection of CO fluorescence from fundamental transitions near 4.7 μm ; (2) excitation of CO₂ via the $(20^0_1)_{II} \leftarrow (00^0_0)$ band near 5000 cm^{-1} (2.0 μm) and collection of CO₂ ν_3 fluorescence near 4.3 μm ; (3) excitation of the 2ν band of CO followed by rapid CO–CO₂ V-V transfer and collection of CO₂ fluorescence near 4.3 μm . Scheme 1 (Fig 1, left) indicates presence of CO, scheme 2 (Fig. 8) indicates the presence of CO₂, and scheme 3 (Fig 1, right) indicates the presence of both CO and CO₂. Through the use of two cameras,

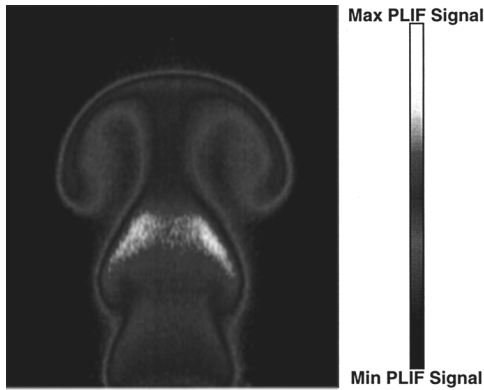


FIG. 8. Single-shot IR PLIF image of a forced 6 mm diameter jet. Jet fluid is 40% CO_2 /60% Ar. 12 mJ excitation of CO_2 at 2.0 μm ; CO_2 fluorescence collected at 4.3 μm . Integration time is 20 μs . Ambient gas is air.

the combination of schemes 1 and 3 allows for simultaneous imaging of both CO and CO_2 with single laser excitation.

Representative peak SNR ratios for room-temperature images (Figs. 1, right, and 8) range from 150 to 200. Signal levels of the images presented here can be used to infer a detection limit (SNR = 1) for the present experimental setup of 1350 ppm (CO) and 950 ppm (CO_2) at 300 K.

Presentation in these figures is qualitative (color table corresponds to PLIF signal), although it should be noted that techniques and results for quantitative presentation have been presented previously [1].

Flame Demonstrations

A laminar co-flowing CO/Ar/ H_2 flame was used to demonstrate imaging of CO (fuel) and CO_2 (products) in a flame condition. Excitation schemes (1) and (3) were employed. Because the flame generates hot CO and CO_2 which emit within the collection bandwidth, common-mode rejection of flame luminosity was achieved by subtracting an image taken

without laser excitation from the PLIF image. Fig. 9 shows typical CO and CO_2 imaging results. In these images, CO represents fuel and CO_2 represents the fuel-product interface. The fuel region is clearly identified by the CO PLIF signal (which scales with CO concentration), while fuel and product regions are demarcated by the CO_2 signal (which scales with the product of CO and CO_2 concentrations).

Conclusions

We have presented IR PLIF techniques, analysis, and demonstrations for imaging of CO and CO_2 . Calculations of fluorescence yield indicate that while infrared techniques suffer from weak spontaneous emission rates, the slow nature of most nonresonant VET processes make the fluorescence yield suitably high for imaging with favorable SNRs. In addition, these VET processes enable imaging of more than one species with a single excitation laser. Detailed VET modeling has been used to design engineering models for the fluorescence yield ϕ ; in the simplest case, short exposures can be used to make ϕ roughly constant throughout an image. PLIF imaging of CO and CO_2 has been demonstrated at 10 Hz acquisition rate with minimum detection limits near 1000 ppm (CO) at 300 K. Images of CO and CO_2 in a steady laminar co-flowing CO/Ar/ H_2 flame have also been presented, showing that use of two well-calibrated InSb focal planes can successfully achieve common-mode rejection of flame luminosity. Given that our laser system provides output ranging from 1.3 to 4.7 μm , opportunities exist to extend these measurements to other combustion species such as H_2O and CH_4 . Potential application includes imaging of preflame (fuel) regions of lifted flames and imaging of mixing processes associated with exhaust reinjection in internal combustion engines.

Acknowledgments

This research was supported by the Air Force Office of Scientific Research, Aerospace and Materials Sciences Directorate, with Dr. Julian Tishkoff as technical monitor.

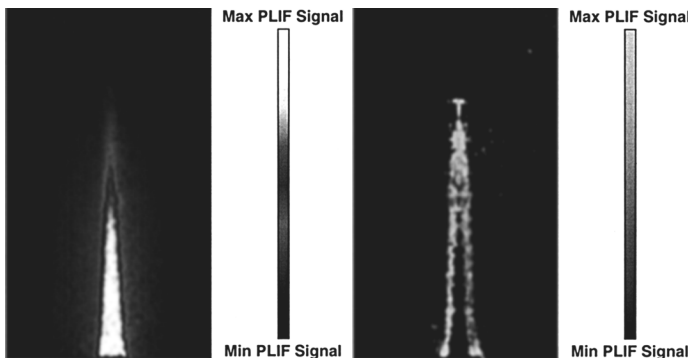


FIG. 9. CO (left) and CO_2 PLIF images upon excitation of the R(12) line of CO for a steady laminar co-flowing CO/ H_2 flame. Signal at left indicates the presence of CO (fuel); signal at right indicates the presence of both CO and CO_2 (fuel-product interface).

REFERENCES

1. Kirby, B., and Hanson, R., *Appl. Phys. B* 69(5/6):505–507 (1999).
2. Seitzman, J., and Hanson, R., in “Planar Fluorescence Imaging in Gases,” *Experimental Methods for Flows with Combustion* (A. Taylor, ed.), Academic Press, London, 1993.
3. Kohse-Hoinghaus, K., *Prog. Energy Combust. Sci.* 20(3):203–279 (1994).
4. Long, M., Fourquette, D., and Escoda, M., *Opt. Lett.* 8(5):244–246 (1983).
5. Barlow, R., Frank, J., and Fiechtner, G., paper WSS/CI 98S-19, Western States Section Spring Meeting of the Combustion Institute, University of California, Berkeley, California, March 23–24, 1998.
6. Haumann, J., Seitzman, J. M., and Hanson, R. K., *Opt. Lett.* 11(12):776–778 (1986).
7. Juhlin, G., Neij, H., Versluis, M., Johansson, B., and Alden, M., *Combust. Sci. Technol.* 132(1/6):75–97 (1998).
8. Millikan, R., and White, D., *J. Chem. Phys.* 39(12):3209–3213 (1963).
9. Starr, D. F., Hancock, J. K., and Green, W. H., *J. Chem. Phys.* 61(12):5421–5425 (1974).
10. Price, T. C., Allen, D. C., and Simpson, C., *Chem. Phys. Lett.* 53(1):182–184 (1978).
11. Allen, D. C., Price, T. J., and Simpson, C., *Chem. Phys.* 41(3):449–460 (1979).
12. Cacciatore, M., and Billing, G. D., *Chem. Phys.* 58(3):395–407 (1981).
13. Powell, H. T., *J. Chem. Phys.* 63(6):2635–2645 (1975).
14. Billing, G. D., *Chem. Phys.* 50(2):165–173 (1980).
15. Cacciatore, M., Capitelli, M., and Billing, G. D., *Chem. Phys.* 89(1):17–31 (1984).
16. Chakroun, A., Margottin-Maclou, M., Gueguen, H., Doyennette, L., and Henry, L., *Comptes Rendus Hebdomadaires Des Seances De L Academie Des Sciences Serie B* 281(1):29–32 (1975).
17. Starr, D. F., and Hancock, J. K., *J. Chem. Phys.* 63(11):4730–4734 (1975).
18. Taine, J., Lepoutre, F., and Louis, G., *Chem. Phys. Lett.* 58(4):611–615 (1978).
19. Taine, J., and Lepoutre, F., *Chem. Phys. Lett.* 65(3):554–558 (1979).
20. Taine, J., and Lepoutre, F., *Chem. Phys. Lett.* 75(3):448–451 (1980).
21. Doyennette, L., Margottin-Maclou, M., Chakroun, A., Gueguen, H., and Henry, L., *J. Chem. Phys.* 62(2):440–447 (1975).
22. Finzi, J., and Moore, C. B., *J. Chem. Phys.* 63(6):2285–2288 (1975).
23. Lepoutre, F., Louis, G., and Taine, J., *J. Chem. Phys.* 70(5):2225–2235 (1979).
24. Taine, J., and Lepoutre, F., *Chem. Phys. Lett.* 75(3):452–455 (1980).
25. Billing, G. D., *Chem. Phys.* 67(1):35–47 (1982).
26. Jolicard, G., and Perrin, M. Y., *Chem. Phys.* 123(2):249–265 (1988).
27. Billing, G. D., and Fisher, E. R., *Chem. Phys.* 43(3):395–401 (1979).
28. Billing, G. D., and Kolesnick, R. E., *Chem. Phys. Lett.* 200(4):382–386 (1992).
29. McMillin, B. K., Palmer, J. L., and Hanson, R. K., *Appl. Opt.* 32(36):7532–7545 (1993).

COMMENTS

Larry Rahn, Sandia National Laboratories, USA. Will you please comment on the limitations imposed on IR PLIF by optical density or trapping effects? Especially, for the relatively high species concentrations proposed and/or detectable.

Author's Reply. Radiative trapping places a limit on the physical dimensions of flows which can be visualized because the fluorescence from CO or CO₂ is resonant with absorption transitions of those species and the attendant absorption generates spatially-dependent signal attenuation. Effects of signal attenuation are reduced by using cold gas filters to reject emission from transitions to the ground state, thus collecting only hot transitions for which lower state populations are smaller and therefore absorption is weaker. For results in this presentation, radiative trapping produces errors below 5%. At typical flame conditions, errors may be kept below 10% through 2 cm pathlengths.

G. Gruenefeld, University of Bielefeld, Germany. What about using CO or CO₂ overtone lasers for excitation? Also, how does interference with H₂O absorption affect the detection limits of CO in typical exhaust gases?

Author's Reply. Since CO lasers operate on transitions in an excited electronic state, CO laser transitions are in general not resonant with the absorption lines of ground electronic state CO.

Water absorption does not affect detection limits for CO in exhaust. Since this is a fluorescence technique, the requirement for absorption interferences is only that they not appreciably attenuate the laser. The absorbance of the visualized species need not dominate over that of an interfering species. Furthermore, water absorption at 2.3 microns is relatively minor, and this window is a good one for probing CO with minimal water interference [1].

REFERENCE

1. Webber, M. E., Wang, J., Sanders, S. T., Baer, D. S., and Hanson, R. K., *Proc. Combust. Inst.* 28:407–413 (2000).

